

JGR Planets

RESEARCH ARTICLE

10.1029/2024JE008875

Key Points:

- · We successfully simulated the formation of the largest fresh crater observed to have formed on Mars using iSALE3D shock physics code
- The most likely impact scenario is a 6m-wide impactor striking a 15-m thick regolith overlaying fractured bedrock at 12 km/s at 20°
- The water ice observed in proximal ejecta originated from depths 3.2-11 m, and was laterally discontinuous under the preimpact surface

Supporting Information:

Supporting Information may be found in the online version of this article.

Correspondence to:

N. Wójcicka and G. S. Collins, n.wojcicka18@imperial.ac.uk; g.collins@imperial.ac.uk

Citation:

Wójcicka, N., Collins, G. S., Rangarajan, V. G., Dundas, C. M., & Daubar, I. J. (2025). Origins of the water ice excavated by the Christmas Eve crater formation on Mars. Journal of Geophysical Research: Planets, 130, e2024JE008875, https://doi. org/10.1029/2024JE008875

Received 19 DEC 2024 Accepted 7 AUG 2025

Author Contributions:

G. S. Collins

Conceptualization: N. Wójcicka,

G. S. Collins Formal analysis: N. Wójcicka, V. G. Rangarajan Investigation: N. Wójcicka, C. M. Dundas Methodology: N. Wójcicka, G. S. Collins, V. G. Rangarajan, I. J. Daubar Supervision: G. S. Collins Validation: C. M. Dundas, I. J. Daubar Visualization: N. Wójcicka Writing - original draft: N. Wójcicka,

© 2025. The Author(s). This article has been contributed to by U.S. Government employees and their work is in the public domain in the USA. This is an open access article under the

terms of the Creative Commons Attribution License, which permits use, distribution and reproduction in any medium, provided the original work is properly cited.

Origins of the Water Ice Excavated by the Christmas Eve **Crater Formation on Mars**

N. Wójcicka¹, G. S. Collins¹, V. G. Rangarajan², C. M. Dundas³, and I. J. Daubar⁴



¹Department of Earth Science and Engineering, Imperial College London, London, UK, ²Institute of Planetary Research, German Aerospace Center (DLR), Berlin, Germany, ³U.S. Geological Survey, Astrogeology Science Center, Flagstaff, AZ, USA, ⁴Brown University, Providence, RI, USA

Abstract On the 24th of December 2021, a meteoroid struck the martian surface, producing a 150-m wide crater and excavating the lowest-latitude water ice observed on Mars to date. Knowledge of the preimpact depth, thickness and lateral continuity of the excavated ice would provide new insight into past environmental changes such as temperature and humidity of the atmosphere. In this work, we use the iSALE3D shock physics code to simulate the crater formation and constrain both the impact parameters and the original location of excavated ice. Analysis of the distal ejecta pattern suggests that the impact angle was $20 \pm 2.5^{\circ}$ from horizontal. Based on a comparison of the simulated and observed crater morphology, we find the preimpact subsurface likely contained a stronger bedrock layer overlain by 15 m thick regolith layer. Our simulation results show that the ejected ice blocks visible in orbital images originated from shallow depths 3.2-11 m and from radii 30-60 m from the crater center. We conclude that the ice most likely originated from a massive ice layer at 3.2-11 m depth. The ice was likely also laterally discontinuous under the preimpact surface.

Plain Language Summary On the 24th of December 2021, a meteoroid struck the martian surface, producing a 150-m wide crater. The impact uncovered water ice in a region nearest to the equator observed on Mars to date. We used computer simulations of the formation of the crater to understand the meteoroid's and subsurface properties. We constrain the impact angle to be $20 \pm 2.5^{\circ}$ from horizontal. We find that the ice most likely originated from a patchy ice layer at a depth of 3.2–11 m under the preimpact surface. We also conclude that the preimpact subsurface contains a stronger fractured bedrock layer at 15 m depth, which is overlain by weak regolith.

1. Introduction

On the 24th of December 2021 (at approximately 18:49 LMST, Ls = 147, Posiolova et al., 2022, Mars year 36 Piqueux et al., 2015), a meteoroid struck the martian surface in Amazonis Planitia (35.1°N, 189.82°E), producing a 150-m wide crater. The blast pattern produced by the impact extends up to 37 km from the crater (Posiolova et al., 2022). The impact excavated water ice, representing the lowest-latitude water ice excavated by a meteoroid impact observed on Mars to date (Dundas et al., 2023). Finding the lowest-latitude ice deposits provides insights into the history of deposition and removal of subsurface ice, due to changes in climate conditions, such as temperature, atmospheric water content and variations in orbit and obliquity of the planet (Dundas et al., 2023). As this crater is also the largest fresh crater located on Mars since MRO (Mars Reconnaissance Orbiter) began operations (Posiolova et al., 2022), it provides an excellent opportunity to inform those constraints. Knowing the origin depth and thickness of the ice can therefore help inform our understanding of the climate history of Mars. The presence of massive ice at shallow depths excavated by the impact would suggest more stable conditions for water ice in recent history. On the other hand, discontinuous or pore-filling ice would suggest more climate variability, with stable and unstable intervals represented in the geologic record (Dundas et al., 2023).

The seismic waves produced by this impact were recorded by InSight's (Banerdt & Russell, 2017, Interior Exploration using Seismic Investigations, Geodesy and Heat Transport) seismometer SEIS (Lognonné et al., 2019, Seismic Experiment for Interior Structure) 3,500 km away, and it was determined to be the source of event S1094b (named following InSight event naming convention; InSight Marsquake Service, 2023). At magnitude 4.0, the impact produced one of the largest and most distant seismic events detected by InSight, therefore providing crucial information about the internal structure of Mars (e.g., crustal density and thickness, Kim et al., 2022). It is also the largest impact seismically detected by InSight (Posiolova et al., 2022). Whilst

WÓJCICKA ET AL. 1 of 16 Writing – review & editing: N. Wójcicka, G. S. Collins, V. G. Rangarajan, C. M. Dundas, I. J. Daubar previous studies have investigated impact-generated seismic waves using shock physics numerical modeling (Froment et al., 2020, 2020, 2024; Rajšić et al., 2021; Wójcicka et al., 2020) and empirical scaling relationships between p-wave amplitude and impact momentum (Garcia et al., 2022; Teanby & Wookey, 2011; Wójcicka et al., 2020), the "Christmas Eve crater" (informally named because the impact occurred on the 24th of December—Christmas Eve) is larger than those considered in those studies, which focused on impacts up to 30 m in crater diameter. In general, the relationship between the impact parameters and the resulting seismic wave parameters is not yet fully understood. Therefore constraining the impact parameters, such as impact momentum, angle and target configuration, for this event is key for calibrating and extending the validity of seismic source models for meteoroid impacts of this scale. As the seismic wave generation is also influenced by the target material, refinement of the preimpact subsurface configuration will aid future efforts to distinguish impacts from other seismic sources.

In this work, we use 3D shock physics numerical modeling with iSALE-3D (Elbeshausen et al., 2009; Elbeshausen & Wünnemann, 2011) to investigate the impact. We first focus on constraining the most likely impact angle, impactor size, and subsurface target structure. We then combine remote sensing, numerical modeling, and data science techniques to constrain depth of origin of the excavated ice and reproduce the likely preimpact distribution of the ice blocks observed around the crater. Our work will provide insight into the thickness, depth, and length-scale of possible discontinuities within sub-surface ice in the region.

2. Observations of the Christmas Eve Crater

2.1. Blast Pattern and Distal Ejecta

The "Christmas Eve crater" is located at 35.1°N, 189.82°E in Amazonis Planitia. Figure 1a shows the CTX (Context Camera; Malin et al., 2007) image (image ID U05_073077_2154_XI_35N170W) of the crater and its distal ejecta. Albedo change produced by the impact is seen up to ≈ 37 km from the crater (seen as the darkened region in Figure 1a). The blast zone shows an uprange forbidden zone. The presence of a forbidden zone uprange but not downrange suggests an oblique impact angle of $35-20^{\circ}$ (Gault & Wedekind, 1978; Posiolova et al., 2022). Sharp "scimitars" (CTX image, Figure 1a) are visible on both sides of the crater up to approximately 18 km toward the northwest and southwest (in the uprange direction) (Posiolova et al., 2022). They are hypothesized to be formed by interaction of the hemispherical atmospheric blast wave generated by the ground impact and the cylindrical blast wave (Mach cone) generated along the entry trajectory (Burleigh et al., 2012; Ivanov et al., 2020). As shown by Posiolova et al. (2022), the azimuth of the bisection of the angle between the scimitars gives an indication of the impactor's trajectory (55° from north clockwise). As the uprange forbidden zone of the blast pattern is symmetrical along the impactor's path, a separate estimate of trajectory direction can be derived from its width (62° from north clockwise). In this work we use the impact direction derived from the forbidden zone (62°).

2.2. Proximal and Ice Ejecta Distribution

The Christmas Eve impact excavated water ice, with meter-scale blocks observed at roughly all azimuths around the crater. Figure 1b shows the ice patches as white toward the center and blue around the edges. The patches are significantly brighter than the surrounding material. Water ice usually appears "relatively blue" or "relatively white" and brighter than surrounding material in enhanced-color High Resolution Imaging Science Experiment (HiRISE, McEwen et al., 2007) images (Dundas et al., 2023). Whilst the relatively blue color alone is not diagnostic of ice presence, it can be combined with topographical features to detect ice presence in features such as craters (Dundas et al., 2021). The presence of water ice was confirmed through the weak ~1,020 nm characteristic absorption feature in CRISM (Compact Reconnaissance Imaging Spectrometer for Mars) data (Dundas et al., 2023) and through HiRISE color (Rangarajan et al., 2024). At 35°N, this is the lowest-latitude observation of subsurface ice exposed by an impact. The ice is a combination of ice blocks and patches, with the largest blocks up to 3 m wide. This suggests the presence of massive ice in the preimpact subsurface (Dundas et al., 2023).

The ice blocks can be seen even as far away as 700 m from the crater rim (Dundas et al., 2023; Posiolova et al., 2022). The highest concentration of visible ice blocks is contained within 1 crater diameter from the crater rim (Figures 1b and 1c). Here, we define the proximal ejecta blanket as ejecta landing within 1 crater radius from the crater rim and distal ejecta as material landing further away. There is significantly more ice (approximately 4 times the area) visible in the northern half of the proximal ejecta layer. This could be caused by uneven distribution of ice under the preimpact surface.

WÓJCICKA ET AL. 2 of 16

21699100, 2025, 9, Downloaded from https://agupubs.onlinelibrary.wiley.com/doi/10.1029/2024JE008875 by Disch Zentrum F. Luft-U. Raum Fahrt In D. Helmholtz Gemein.

Wiley Online Library on [01/10/2025]. See the Terms and Conditions (https://onlinelibrary

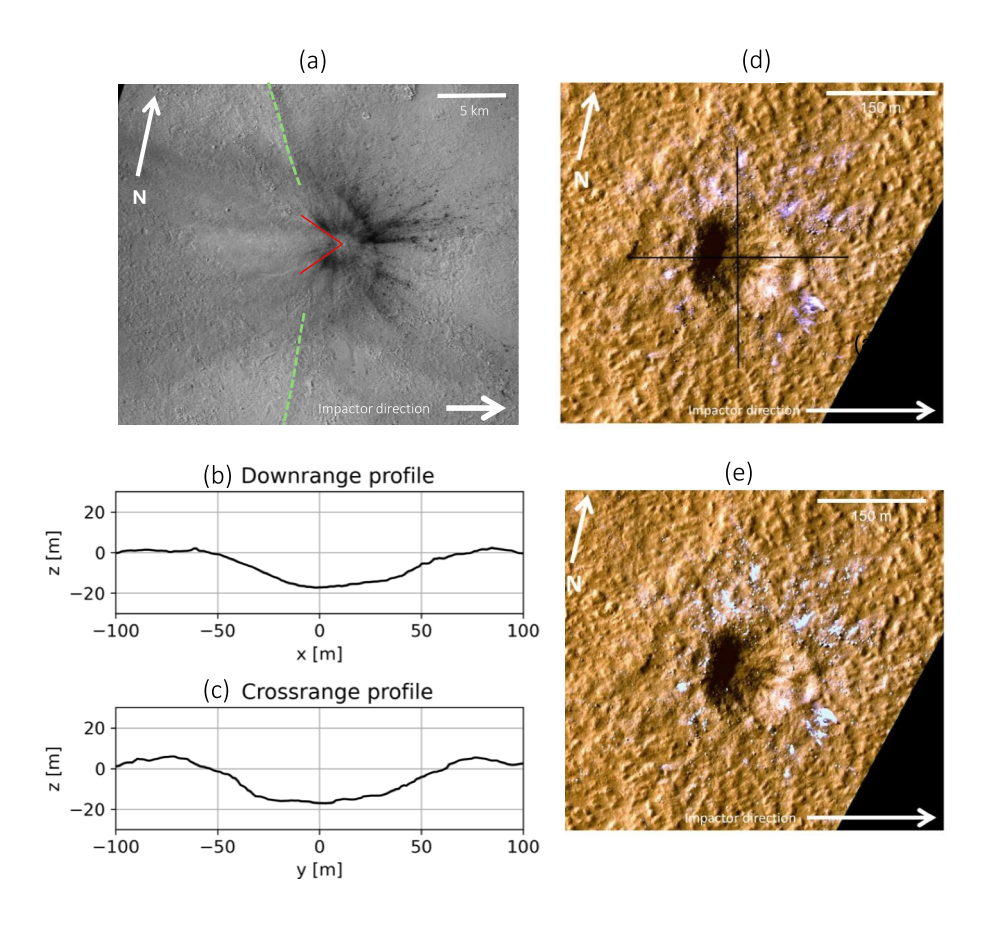


Figure 1. Highlights of the analysis of orbital images of the Christmas Eve crater: (a) CTX image (image ID U05_073077_2154_XI_35N170W) of the Christmas Eve impact crater and the surrounding blast zone. (b) The downrange depth profile along the horizontal black line shown in (b). (c) The crossrange depth profile of the crater along the vertical line shown in (b). (d) HiRISE image (image ID ESP_073077_2155_IRB_A_01_ORTHO) of the crater and the ice-containing ejecta. The black lines mark the downrange and crossrange profiles used to compare the crater morphology with simulation results in this work. (e) The HiRISE image (same as (b)) with ice-containing ejecta (blocks and patches) locations highlighted in light blue. All images were rotated so that the impactor's trajectory is from left to right.

2.3. Crater Morphology

The terrain profile tool in QGIS (QGIS.org, 2024)—an open source Geographical Information System (GIS)—was used on the HiRISE Digital Terrain Model (DTM) of the crater (image ID: DTEEC_073578_2155_073077_2155_A01) to extract the crater depth profiles in along-range and crossrange directions shown in Figures 1d and 1e. The crater is 150 m in diameter, measured at the rim, 21 m deep from the bottom of the crater to the top of the crater rim, and 17 m deep to the preimpact level (Posiolova et al., 2022). The crater is well approximated by a circle of 150 m diameter, and has a flat bottom, particularly well visible in the crossrange profile, suggesting a stronger layer at a depth between 10 and 20 m.

The crater rim is irregular. A "divot" can be observed within the rim approximately in the downrange direction. This could be a consequence of laterally variable layering in the target, a smaller impactor fragment striking the rim during the same impact event or a pre-existing topographical feature. Additionally, similar features have been observed being caused by a ricocheting impactor in shallow impact angle experiments (Gault & Wedekind, 1978).

2.4. Observation Methods—Ice Distribution

CRISM data were previously used to confirm the presence of water ice in the ejecta (Dundas et al., 2023). However CRISM resolution (\approx 18 m per pixel) is significantly lower than that of HiRISE (\approx 0.25–0.5 m per pixel) and larger than the size of most individual ice blocks (<3 m). Therefore our analysis of the ice distribution was restricted to using HiRISE data. To compare the results of our simulations with observations, we produced a map

WÓJCICKA ET AL. 3 of 16

of visible bright patches around the crater that are likely consistent with ice. For this analysis, we utilized the first HiRISE image of the crater (Image ID: ESP_073077_2155), as it likely captures the ejecta at a stage closest to its initial state following crater formation. The UNFILTERED HiRISE data products for this image were first generated by running the HiRISE calibration procedures highlighted in Rangarajan et al. (2024) and Becker et al. (2022) in ISIS (Integrated Software for Imagers and Spectrometers) (Sucharski et al., 2020), followed by the application of an empirical dark subtraction that has been shown to help minimize atmospheric scatter and better retrieve surface signatures (Rangarajan et al., 2023, 2024; Tornabene et al., 2017). Several spectral ratios can be used to identify water ice in HiRISE images. In this work we use the ICE-ATM parameter from Rangarajan et al. (2023). ICE-ATM is defined as the ratio of the mean of all spectral bands to the IR/BG spectral band ratio (Rangarajan et al., 2023, 2024; Tornabene et al., 2017). The ICE-ATM spectral parameter was specifically preferred over the WATER-ICE spectral parameter for this work, as the objective was to generate a map encompassing all bright pixels likely consistent with ice, regardless of its purity. We then calculated and generated the ICE-ATM spectral parameter (Rangarajan et al., 2024) and generate a map selecting pixels with ICE-ATM values above 0.02. The ICE-ATM constraint of 0.02 was selected based on the lowest value of this parameter observed for other confirmed icy mid-latitude craters (Figures 6b and 6c in Rangarajan et al. (2024)).

Figure 1c shows all ejecta locations that are likely consistent with ice, highlighted on the HiRISE image of the crater. Because ice becomes less concentrated farther away from the crater, and therefore more difficult to see and identify with the spectral parameter method, this work focuses on the proximal ejecta containing ice, up to 150 m from the crater center. The total area covered by ice as determined by our method is $\approx 3,300 \text{ m}^2$, which is equal to $\approx 6\%$ of the area considered $(5.3 \times 10^4 \text{ m}^2)$. Tusberti et al. (2024) presented a detailed analysis of the ejecta distribution around the Christmas Eve crater. By manually mapping rocky and icy ejecta up to 564 m (1 km² area) from the crater center, they estimated the total area covered by icy ejecta to be 9, 654 m² (icy boulders only)–12,276 m² (icy boulders and icy patches), which equals $\approx 1\%$ of the area considered. These estimates are 3–4 times larger in area of ice than our estimate, for an area ≈ 18 times larger. As we expect ice-fraction in the ejecta to decrease with ejected range, ice coverage in the area we consider should be several times higher than that of Tusberti et al. (2024). We therefore consider our coverage estimate to be broadly consistent with the analysis of Tusberti et al. (2024).

3. Modeling the Christmas Eve Crater

3.1. Previous Modeling and Open Questions

For exigency, preliminary 2D iSALE modeling of this crater was performed using a single-layer, homogeneous, 25% porous, fractured bedrock target material (Dundas et al., 2023; Posiolova et al., 2022). 2D modeling necessitates simulating a vertical impact. Those models resulted in a crater slightly smaller (130 m in diameter) and much deeper (28 m) than the "Christmas Eve" crater. Whilst the crater morphology was not closely reproduced, the simulations conducted by Dundas et al. (2023) showed that the ice was most likely excavated from depths up to 8 m. However, the ejecta pattern produced from a vertical impact would be symmetrical around the crater, which is not consistent with observations of the uprange forbidden zone. It is therefore not possible to deduce preimpact locations of individual ice-blocks visible in the HiRISE image with a vertical impact simulation.

Observational evidence suggests a more complex impact scenario than this preliminary modeling was able to reproduce: an inhomogeneous target material, and an impact that occurred at a shallow impact angle $\leq 30^{\circ}$ (see Section 2.1). In this work we improve on the previous modeling work by including several more complex, layered target configurations, as well as an oblique impact angle. This approach allows us to more closely reproduce the resulting crater morphology, as well as examine the observed asymmetrical ejecta distribution (in the along-range direction), which could not be reproduced with 2D models. Our 3D models therefore allow us to constrain previously unknown impactor and target parameters, such as target layer configuration, impact angle and pre-impact location of the excavated ice, by comparing our results with observations.

3.2. Numerical Modeling Approach

We used the iSALE-3D shock physics code (Elbeshausen et al., 2009; Elbeshausen & Wünnemann, 2011) to simulate several possible impact scenarios that could represent the formation of the Christmas Eve crater. We varied the impact angle between 15 and 45° , assuming a shallow impact angle ($<45^{\circ}$) based on the observed

WÓJCICKA ET AL. 4 of 16

forbidden zone in the uprange direction and the overall asymmetry of the blast pattern (Posiolova et al., 2022). We repeated each scenario in three target configurations (see Section 3.2.1 for material model description).

The impact velocity for all scenarios was 12 km/s, which is the average impact speed at the top of Mars's atmosphere as atmospheric deceleration of the impactor is not expected to be significant in this case (Posiolova et al., 2022). To achieve approximately the same final crater diameter in each simulation, the impactor mass was increased for shallower impact angles to approximately compensate for the reduction in crater size for the same impact scenario. As crater size is expected to scale with vertical momentum (Elbeshausen et al., 2009), the impactor diameter was varied between 4.8 and 6.6 m, as a function of impact angle, such that the vertical momentum was held constant. The full list of impact scenarios simulated is listed in Table S1 of Supporting Information S1.

The simulation domain was a 3D half-space, with a symmetry plane (x-z) along the impactor's trajectory. In most simulations, the impactor was resolved with 10 cells per projectile radius (CPPR) resulting in individual cell widths between 0.26 and 0.33 m inside the high resolution zone centered on the impact point, depending on the impactor size. In order to prevent pressure wave reflections from the edges of the mesh from affecting the crater formation, we also used extension zones, where the cell width increases by a constant extension factor of 1.05 in each direction outside the high resolution zone. A typical simulation mesh (including high resolution and extension zones) spanned ~400 m (700–750 cells) in the *x*-direction (along range), ~200 m (350–450 cells) in the *y*-direction (cross range) and ~250 m (420–500 cells) in the *z*-direction (vertical). A typical high resolution zone of the simulation mesh spanned ~220 m (600–650 cells) in the *x*-direction (along range), ~100 m (300–350 cells) in the *y*-direction (cross range) and ~110 m (350–400 cells) in the *z*-direction (vertical).

3.2.1. Material Models

The impactor was modeled as a non-porous basaltic sphere, using the Tillotson equation of state for basalt (Tillotson, 1962), with a reference density 2,860 kgm⁻³, and a simple pressure-dependent shear strength model (LUNDD in iSALE) (Lundborg, 1968) with parameters for dense rock. This material model was adopted as a reasonable approximation of the mechanical behavior of stony meteoroids, but because most of the impactor is melted/vaporized during the impact, the details of its material model are not likely to significantly affect the simulation outcomes.

Much of the surface of Mars is covered by a thin layer of weak, porous regolith. Whilst the exact thickness of regolith at the impact site is unknown, analysis of nearby craters suggests that this layer extends 7-40 m beneath the surface (Dundas et al., 2023). To investigate the effect of target layering on crater formation, we employ three alternative target configurations of porous regolith overlaying fractured bedrock with an interface placed at a depth of 10, 15 and 20 m beneath the surface (for each impact scenario in Table S1 of Supporting Information S1). The solid fraction of the fractured bedrock material was modeled using the same Tillotson equation of state for basalt as the impactor (Tillotson, 1962). iSALE's ROCK strength model (Collins et al., 2004) was used to represent the shear response of the bedrock. The fractured bedrock included 25% porosity, accounted for using the $\epsilon - \alpha$ compaction model (Collins et al., 2011; Wünnemann et al., 2006), resulting in bulk density of 2,150 kgm⁻³. The porous regolith was modeled using the Tillotson equation of state for basalt (Tillotson, 1962), combined with the same simple pressure-dependent Lundborg strength model as used for the impactor (Lundborg, 1968) (LUNDD in iSALE) but with parameters appropriate for weak regolith. The shear strength of the regolith was 5 kPa, with an internal friction coefficient of 0.6 and a high-pressure strength limit of 250 MPa. The regolith included a 50% porosity, again using the $\epsilon - \alpha$ compaction model (Wünnemann et al., 2006), resulting in a bulk density of 1,430 kgm⁻³. Both material models were previously used to simulate impacts of small meteoroids on Mars (Rajšić et al., 2021; Wójcicka et al., 2020). A full list of material model parameters can be found in Table S2 of Supporting Information S1.

In this work, we did not explicitly include a distinct ice layer in the target and instead treated ice as a passive observer. Placing an ice layer in our simulations would require prior knowledge of its location, state (massive ice or pore-filling), thickness and depth, which are unknown. In the case that the subsurface ice was discontinuous, and contained both massive and pore-filling ice, it is impossible to know the exact locations of the ice a priori. Tusberti et al. (2024) calculated the total volume of the excavated ice to be 2×10^4 m³, which amounts to approximately 20% of the crater volume. In this work, we assume that the portion of ice excavated during the

WÓJCICKA ET AL. 5 of 16

impact is small enough that it does not strongly influence target rheology. However, as it has been shown that presence of ice affects both crater formation and material ejection in large craters (km-scale) (Sokołowska et al., 2024). For example, a thicker and deeper buried ice layer in the target decreased the ejection velocities and angles. This suggests that the buried ice could be ejected at slower speeds, and therefore land closer to the crater than pure basalt ejecta. Follow-up studies should investigate the effect of ice in 100-m-scale craters, such as the Christmas Eve crater.

3.2.2. Tracking Ejecta

Ejecta were tracked using Lagrangian tracer particles, placed evenly, every 2 high resolution cells, within the high-resolution zone of the simulation domain. Because the fastest moving ejecta is the most likely to be affected by simulation resolution, we ran a suite of shorter simulations (~0.3 s after impact) at a higher resolution of 40 CPPR, to investigate the distribution of the fastest, most distal ejecta (>1 km). As these high-resolution simulations are very computationally expensive, the full length (~7 s after impact) simulations were run at 10 CPPR (see Section 3.2) and used to track the proximal ejecta (<1 km) and the final crater morphology. In total, the number of tracers in the target ranged between 2 and 5 million, depending on the size of the simulation mesh.

The total model time was too short to simulate the ejecta trajectory from ejection to landing, but was sufficient to track the tracer particles until they are ejected from the crater. Tracers were flagged as ejected when they crossed a horizontal plane at a height (h_{ej}) of one impactor radius above the preimpact surface (Raducan et al., 2022). The ejection position (x,y,z) in three dimensions, time of ejection (t_{ej}) , and ejection velocity (v_x,v_y,v_z) of each tracer were also saved. We assumed that after this point, each particle followed a ballistic trajectory and computed the final position of each ejected tracer. We assumed that the effect of the atmospheric drag on the ejecta fragments of interest (1–3 m wide ice blocks) was negligible (Schultz & Gault, 1979), as the ejection velocity of the continuous ejecta blanket is well below terminal velocity for fragments >3 mm. In addition, even particles smaller than this would be unaffected by drag because of the ejecta mass density in the ejecta curtain (Grindrod et al., 2024). The ejecta particles were then projected forward, until they reached the ground again, at landing positions (x_f, y_f, z_f) . The time of flight for each particle was defined as twice the time required to reach the highest altitude. We saved the final and initial positions (provenance) of each tracer particle, as well as several field variables, notably peak pressure and peak temperature experienced by each tracer.

4. Results

Here we present the results of our numerical simulations and compare them with observations of the Christmas Eve crater. First, we compare the simulated distribution of distal ejecta with the observed blast pattern in order to constrain the impact angle. We then consider crater morphology to help constrain the target configuration, before presenting our predictions of ice provenance and most likely preimpact ice distribution.

4.1. Distal Ejecta Pattern

Figure 2 shows the simulated distal ejecta (r > 1 crater radius from crater rim) distribution at their final landing locations at distances up to 15 km from the crater. Posiolova et al. (2022) used residual albedo analysis to locate the uprange ejecta forbidden zone and measured its width to be 70° (red lines in Figure 2) at a range of 1–2 km from the crater. The ejecta distribution most compatible with this result is achieved by our simulation of impact at 20°. A shallower impact angle (15°) produces a much wider forbidden zone than that of the Christmas Eve crater, and a steeper (25°–45°) impact angle produce a narrower forbidden zone with an inner edge that is much further away from the crater.

The scimitars visible in the CTX image of the blast zone are also marked in Figures 2b-2f (green dashed lines). The results of our simulations show that the location and shape of the scimitars could also be consistent with the uprange edge of the ejecta blanket for an impact at an angle of $20^{\circ} \pm 5^{\circ}$. The uncertainty is based on the steeper and shallower impact angles being incompatible with observations. This could indicate an alternative scimitar formation mechanism by ejecta deposition or interaction between the ejecta and the ground and/or atmosphere. If the scimitar streaks are indeed related to the ejecta blanket emplacement, this further supports the conclusion that the Christmas Eve crater was most likely formed by an impact at an angle of 20° . We therefore focus subsequent analysis on the simulations at this impact angle.

WÓJCICKA ET AL. 6 of 16

21699100, 2025, 9, Downloaded from https://agupubs.onlinelibrary.wiley.com/doi/10.1029/2024JE008875 by Disch Zentrum F. Luft-U. Raum Fahrt In D. Helmholtz Gemein.,

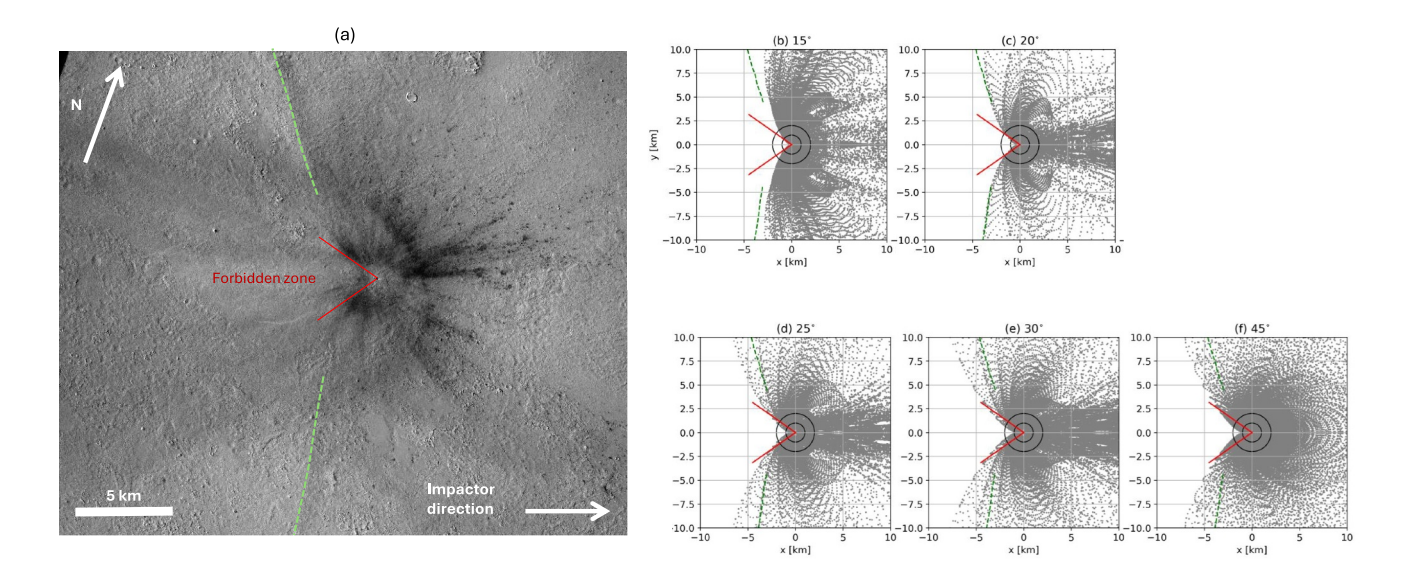


Figure 2. (a) Blast zone around the Christmas Eve crater observed in CTX image (image ID U05_073077_2154_XI_35N170W). Red lines mark the observed uprange forbidden zone (70° wide, Posiolova et al., 2022). (b–f) Distal ejecta blanket for impacts into 15-m-thick regolith layer, at impact angles between 15° and 45°. Red lines mark the observed uprange forbidden zone from (a), determined between 1 and 2 km from the crater (marked with black circles). Green dashed lines show the location of the scimitars visible to the north and south of the impactor's trajectory.

4.2. Crater Morphology and Target Configuration

Each iSALE3D simulation ran for 6–8 s model time. The internal crater profiles at the end of simulations with an impact angle of 20° into each target configuration are shown in Figure 3, to illustrate the dependence of crater morphology on target material. A topographic trace of the observed crater cross-section from the HiRISE DTM is also shown on each panel. Note that we only present the crater profiles for each target configuration for a single impact angle to illustrate the key differences, which are common between other impact angles investigated.

The simulation at 20° into a shallow regolith layer (10 m thick, Figures 3a and 3d) resulted in a crater of diameter between 106 and 110 m (measured at preimpact surface) or 125–129 m (measured at the crater rim). This crater diameter is slightly smaller than the observed crater, which suggests that in this case the choice of impactor mass was too small. The depth of the simulated crater at the deepest point is 15 m below the preimpact surface, which is quite consistent with observation. However, if a larger impactor mass was used to achieve a wider crater, it is likely that the crater depth would increase by approximately the same proportion and give a final simulated crater that is slightly deeper than observed. Moreover, the presence of the thin 10-m regolith layer results in a "ledge" in

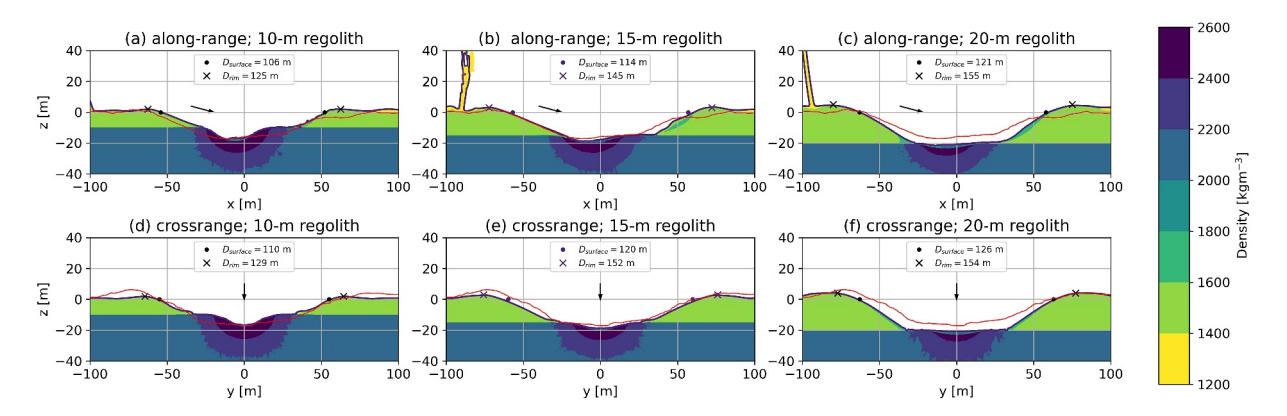


Figure 3. Final save time of a simulated impacts at 20° into (a, d) 10 m regolith layer, (b, e) 15 m regolith layer and (c, f) 20 m regolith layer. A topographic trace of the observed crater cross-section is also shown on each panel as a thin red line. The dot and cross markers show where the crater sizes were measured for each crater. Arrows indicate the impactor's trajectory and impact point on each panel.

WÓJCICKA ET AL. 7 of 16

21699100, 2025, 9, Downloaded from https://agupubs.onlinelibrary.wiley.com/doi/10.1029/2024JE008875 by Disch Zentrum F. Luft-U. Raum

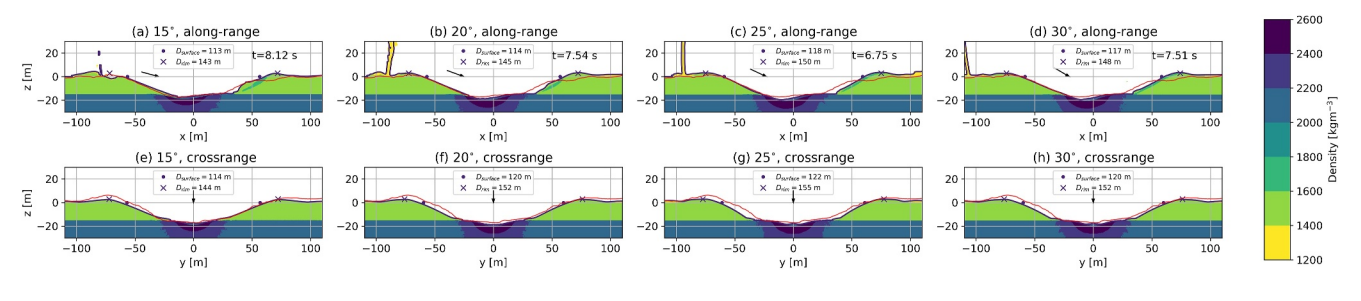


Figure 4. The simulated crater profiles recorded at the last save time of each simulation for impact angles 15°–30°, into a fractured bedrock layer overlain by a 15-m thick porous regolith layer. The profiles are shown in (a–d; top row) along-range direction and (e–h; bottom row) crossrange direction. Observed crater profile is shown as solid red line for comparison in each panel. The markers show where the crater diameter was measured at the preimpact surface level (dots) and at the crater rim level (crosses), and the respective crater diameters are also given on each panel. Impact direction is left to right (top panels) and into the page in (bottom panels). Arrows indicate the impactor's trajectory and impact point on each panel.

the crater wall, formed most prominently on the downrange side and extending around the entire rim (seen at depth of 10 m in Figures 3a and 3d). Such a ledge is not identifiable in the morphology of the observed crater. Thus, this is not the favored target configuration.

The simulation at 20° into the 20 m-thick regolith layer (Figures 3c and 3e) yielded a crater with a flat-floor morphology similar to the observed crater. The crater diameter is consistent with the Christmas Eve crater: 121–126 m at preimpact surface and 155–154 m at the crater rim. However, at 20–22 m depth, the crater is significantly deeper than the observed crater. Again, if a slightly smaller impactor mass (or lower impact speed) were used to achieve a shallower crater, the crater diameter would decrease by approximately the same proportion and give a final simulated crater that is smaller than observed.

Our simulation at 20° impact angle into the 15-m thick regolith layer (Figures 3b and 3f) produced a crater of diameter between 121 and 124 m (measured at the preimpact surface) or 148–152 m (measured at the crater rim), consistent with the observed crater size. The simulated crater is 17–20 m deep (measured at the deepest point), also in agreement with the observed depth of 17 m from the deepest point to the preimpact surface. The sides of the simulated crater show similar slope angles to those of the Christmas Eve crater, with the exception of the left crater wall in the crossrange profile, which appears to be less steep than observed, with a slightly less pronounced crater rim on that side. This could be an indication of lateral variation in layering in the target subsurface. Based on the consistent crater diameter and depth, we therefore conclude that the most probable target configuration of the preimpact subsurface is a 15 m deep porous regolith layer overlaying a stronger, fractured bedrock layer.

Craters resulting from impacts at different impact angles into the 15-m regolith layer target configuration (as shown Figure 4) do not vary substantially in morphology from those shown in Figure 3. This suggests that, in the impact angle range investigated here, impact momentum and regolith depth are the key parameters that control crater morphometry. Crater morphology therefore does not provide strong evidence to further constrain the impact angle that is most likely to have formed the Christmas Eve crater. Our results are consistent with an impact angle of 20° constrained by the distal ejecta deposit.

4.3. Proximal Ejecta Distribution

As we do not explicitly simulate the presence of ice in this work, we use the bulk response of the regolith material during impact to estimate where the solid blocks of ice observed in the ejecta could have been located prior to impact. To remain as solid blocks, the ice must not have experienced a pressure greater than 10 MPa (the typical unconfined compressive strength of ice (Durham et al., 1983)) or a temperature greater than 0°C (the melting point of pure ice). While our regolith material model accounts for the bulk effect of pore crushing on impact heating, it does not account for the presence of ice within the pores or localized hot-spot heating owing to pore collapse, which will both lower the shock pressure required to melt pore ice. To partially address this limitation, we use a regolith peak-shock temperature (rather than the post-shock temperature) of 0°C as the threshold for melting ice within it. This corresponds to a shock pressure of approximately 0.46 GPa, which is larger than the threshold for the crushing of ice. Hence, in practice we defined an ejected tracer as "ice-compatible" if the material did not experience a pressure greater than 10 MPa.

WÓJCICKA ET AL. 8 of 16

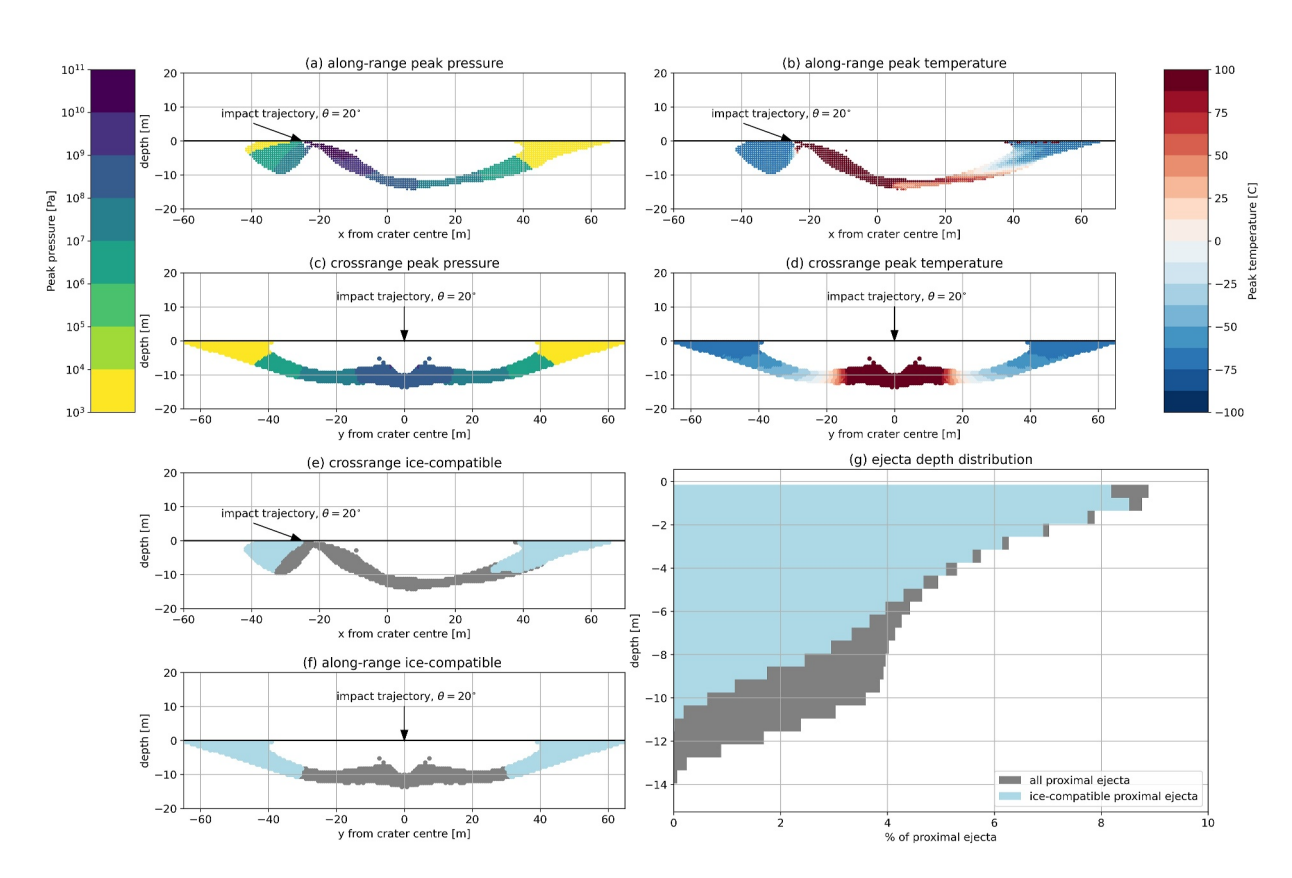


Figure 5. Preimpact locations of simulated proximal ejecta for impacts into 15-m-thick regolith layer, at impact angle of 20° from horizontal, shown as a cross-section of a 10-cell-wide slice through the center of the crater. (a, b) The along-range profile. (c, d) The crossrange profile. Panels (a, c) show ejecta colored by peak pressure experienced during the impact. Panels (b, d) show ejecta colored by peak temperature experienced during the impact. Panels (e, f) show the ice-compatible ejecta tracers $(P_{peak} < 10 \text{ MPa} \text{ and } T_{peak} < 0^{\circ})$ (c) colored in light blue and the melted/crushed proximal ejecta tracers in gray. The tracers are plotted in a crater-centric frame of reference. The impactor's trajectory is marked with a black arrow, ending at the impact point. (g) The percentage of proximal ejecta originating from all depths, colored by ice-compatible (light blue) and melted/crushed (gray).

The provenance (preimpact location) of the proximal ejecta tracers is shown in Figures 5a–5d, as a 10-cells-wide cross-section through the center of the crater (in the along-range and crossrange direction), colored by peak temperature and pressure experienced by each tracer. The area where the impactor penetrates the target experienced the highest temperatures and pressures. For all impact angles, 70%–80% of simulated tracers in the proximal ejecta blanket were ice-compatible, as defined by the above temperature and pressure criteria. However, based on the estimated volume of excavated ice (6% by area), the actual proportion of ice in the ejecta blanket is much less than 70%–80%. The discrepancy between that number and the volume of ice from observations of the crater suggest that only a small portion of the material landing in those areas actually contained ice. This suggests a large uncertainty of the exact ice location within the pre-impact target. The ice-compatible tracers are shown in Figure 5 in light green and yellow (low peak pressure region; panels (a) and (c)), and blue (low peak temperature region; panels (b) and (d)).

The provenance of ice-compatible and ice-incompatible (crushed/melted) proximal ejecta is also shown in Figures 5e and 5f. Gray markers show material that would be melted or crushed if it were ice, and therefore could not have contained the ice blocks visible in the orbital observations around the crater. Blue markers show the ice-compatible ejecta, as defined above. Note that ice-compatible tracers serve as markers of where ice could have been located and survived as blocks to be visible, not necessarily where ice was located.

The bar chart in Figure 5g shows the proportion of all proximal ejecta (gray + light blue) that originated from a given depth, as well as the relative proportion of ice-compatible (light blue) and ice-incompatible (gray) ejecta. Note that these are expressed as proportions of all proximal ejecta, including those further than 10 cells from the symmetry plane and not shown on the other panels. This gives an indication of the likelihood that the visible ice originated from a given depth. Proximal ejecta originated from depths up to 12 m, while ice-compatible material

WÓJCICKA ET AL. 9 of 16

21699100, 2025, 9, Downloaded from https://agupubs.onlinelibrary.wiley.com/doi/10.1029/2024JE008875 by Disch Zentrum F. Luft-U. Raum Fahrt In D. Helmholtz Gemein.,

Wiley Online Library on [01/10/2025]. See the Terms and Conditions (https://

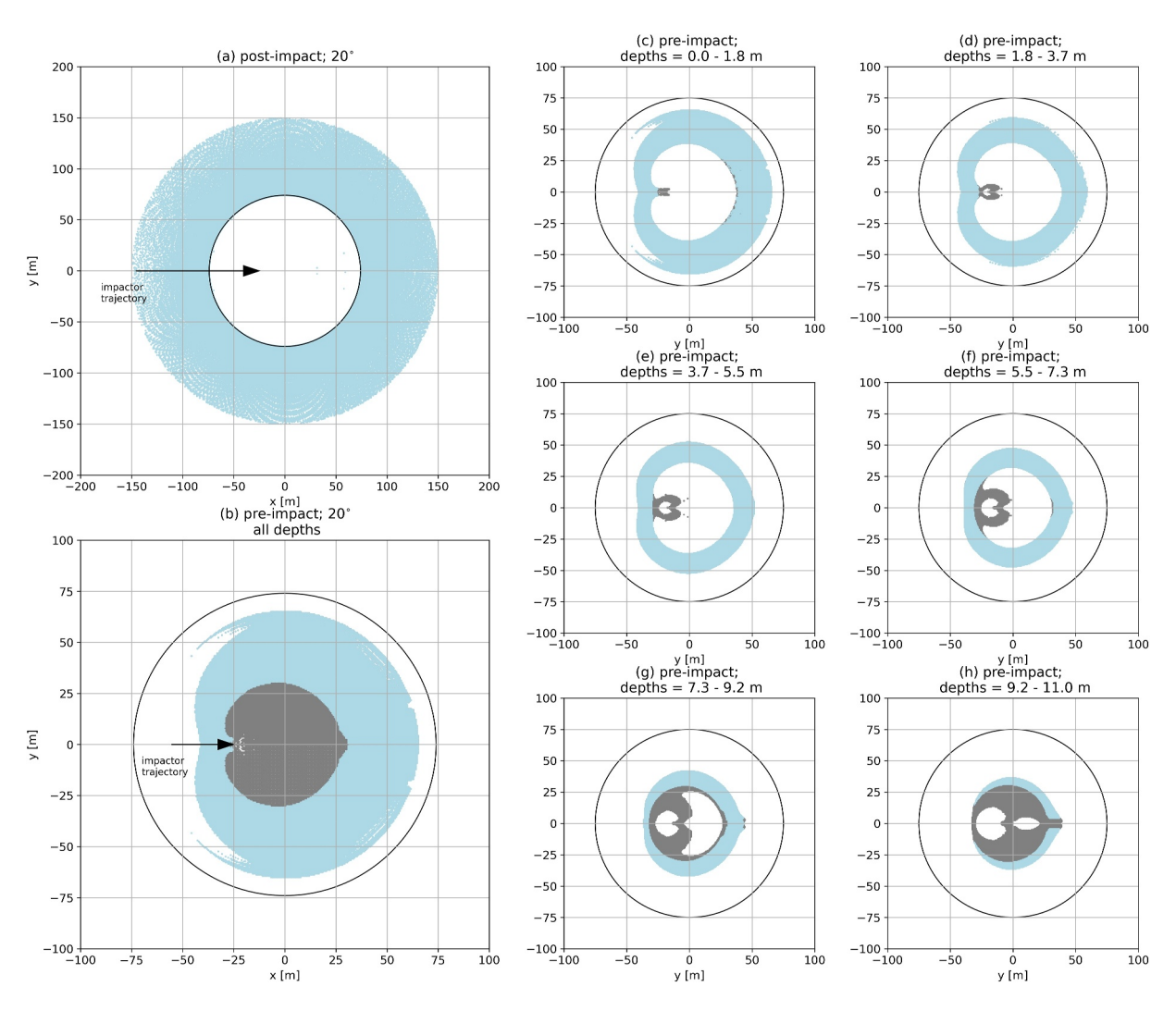


Figure 6. (a) Post-impact locations of simulated ice-compatible proximal ejecta (light blue) around the crater for impact into 15-m-thick regolith layer, at impact angle of 20°. Between 70% and 80% of the proximal ejecta is compatible with ice. (b) Preimpact locations of the proximal ejecta blanket shown inside the crater rim, in light blue for ice-compatible ejecta and in gray for ice-incompatible ejecta. Black arrows indicate impactor's trajectory and impact point. (c-h) Preimpact locations of simulated proximal ejecta shown as 1.8 m thick slices in depth. Ice-compatible ejecta is shown in light blue, and ice-incompatible ejecta is shown in gray. Approximate crater rim is shown on each panel as a black circle.

originated from depths up to 11 m. For a 20° impact angle, over 90% of all proximal ejecta that originated above a depth of 5.6 m is ice-compatible.

The plan view of the post-impact proximal ejecta distribution for the simulation with an impact angle of 20° into a 15-m-thick regolith target is shown in light blue in Figure 6a. This produces an approximately uniform distribution of ejecta around the crater, up to 150 m from crater center. The uprange forbidden zone observed in the distal ejecta is not present in the proximal ejecta. The plan-view provenance of the proximal ejecta tracer particles is shown in Figure 6b. Ice-compatible ejecta originates from an annulus-shaped area 30–60 m from the crater center (light blue). Any ice material ejected from closer to the center is either melted, crushed, or ejected farther than 150 m. Material ejected from outside this area lands on the inner flank of the rim above the preimpact surface. Figures 6c–6i show the provenance of the ejecta tracer particles that originate from 1.8-m-thick slices with depth. The light blue regions therefore indicate where the excavated solid ice could have originated from, as a function of depth. The maximum width of potential subsurface blocks of ice varies with depth, indicated by the thickness of the light blue region on each panel. If the excavated ice originated from nearer the surface, individual blocks could be as wide as ≈ 15 m. This width is reduced to ≤ 10 m, if the ice was excavated from depths 9–11 m. These maximum widths can easily explain the 3-m dimension of the largest observed ice block.

WÓJCICKA ET AL. 10 of 16

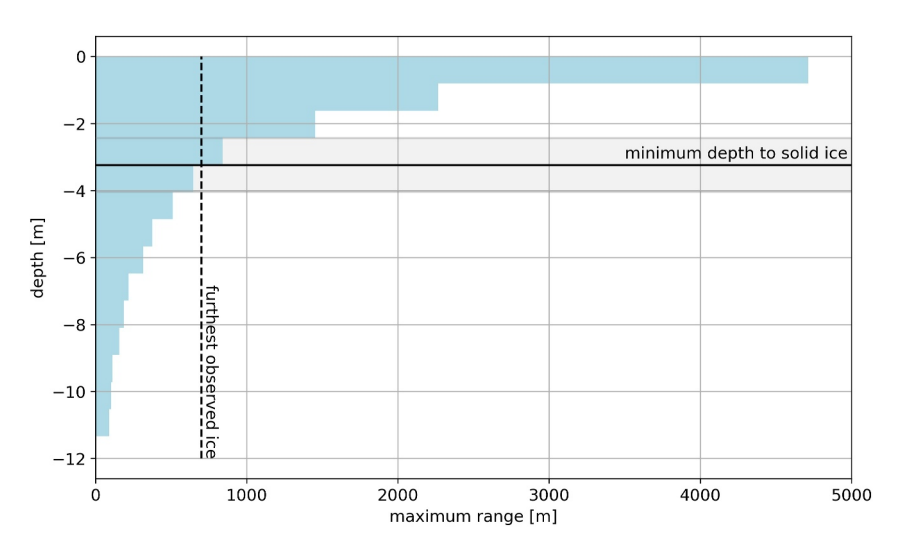


Figure 7. Maximum range of simulated ice-compatible material ejected from a given depth for the impact angle of 20°, in increments of 0.8 m depth. The black dashed vertical line indicates the maximum distance where icy ejecta was observed around the Christmas Eve crater (700 m). The solid black line shows the minimum depth to massive ice with uncertainty marked with gray lines and shading.

4.4. Preimpact Ice Distribution

To better constrain where the ice blocks in the Christmas Eve crater's ejecta originated, we use the orbital observations. We first examine the maximum range of ejecta from different depths. In general, the shallowest material is ejected the furthest, and the maximum range of material decreases with increasing depth. In the case of the Christmas Eve crater, icy ejecta was observed up to \approx 700 m from the crater (Dundas et al., 2023). Figure 7 shows the maximum range of ice-compatible ejecta as a function of depth in 0.8 m increments. The black vertical line marks 700 m—the distance up to which ice was observed. Assuming that the ice blocks originated from a massive ice layer, a shallow ice layer (0–3 m depth) would produce ice-compatible ejecta up to 5 km from the crater, suggesting that ice blocks should be visible much further than they are observed. On the other hand, a very deep layer of ice (below 5 m) would only reach \approx 500 m from the crater, which is closer than the furthest observed ice. Our simulations therefore suggest that the minimum depth to massive ice is 3.2 ± 0.8 m (dotted line in Figure 7). The secondary crater morphology also independently indicates a depth to ice of 1 m (but greater in places) (Dundas et al., 2023). The uppermost ice may be pore ice, not massive ice, which would not be visible in HiRISE images.

Next, we use this depth information to determine a possible preimpact distribution of individual ice blocks around the crater. In Figure 8a, we plot the simulated ice-compatible tracers at their landing locations (light blue), overlain by the observed locations of ice from Figure 1c (dark blue and red). We then select the proximal ejecta tracers that overlap a pixel containing ice (dark blue). The overlap here is defined as within eight high-resolution simulation cells (8 simulations cells = 2.1 m, for the simulation at 20° impact angle) in x- and y-directions from the center of each ice pixel. The small number of pixels with no overlapping tracers are marked in red. Overall, 99% of ice-containing pixels overlap at least one simulated ejecta tracer, for an impact angle of 20° .

The tracers overlapping ice blocks are then plotted at their positions at the start of the simulation in Figure 8b. The resulting distribution shows the possible configuration of ice under the preimpact surface. Figures 8c–8h illustrate the provenance of the overlapping tracers with depth, in 1.3-m-thick slices. The preimpact ice distribution for all depths is laterally discontinuous, particularly in the southern portion of the crater. The patches appear to be up to 15 m in length (depending on depth) and originate from depths 3.2–11 m depth, which could indicate the presence of buried massive ice several meters thick, consistent with Dundas et al. (2023). This is consistent with the largest blocks visible in orbital images (<3 m). The overlapping tracers originating from the upper layers of the target are more laterally dispersed and patchy than those originating deeper. They also originate closer to the crater rim than those from deeper within the target.

WÓJCICKA ET AL. 11 of 16

21699100, 2025, 9, Downloaded from https://agupubs.onlinelibrary.wiley.com/doi/10.1029/2024E1008875 by Disch Zentrum F. Luft-U. Raum Fahrt In D. Helmholtz Gemein., Wiley Online Library on [01/10/2025]. See the Terms and Conditions Ontros

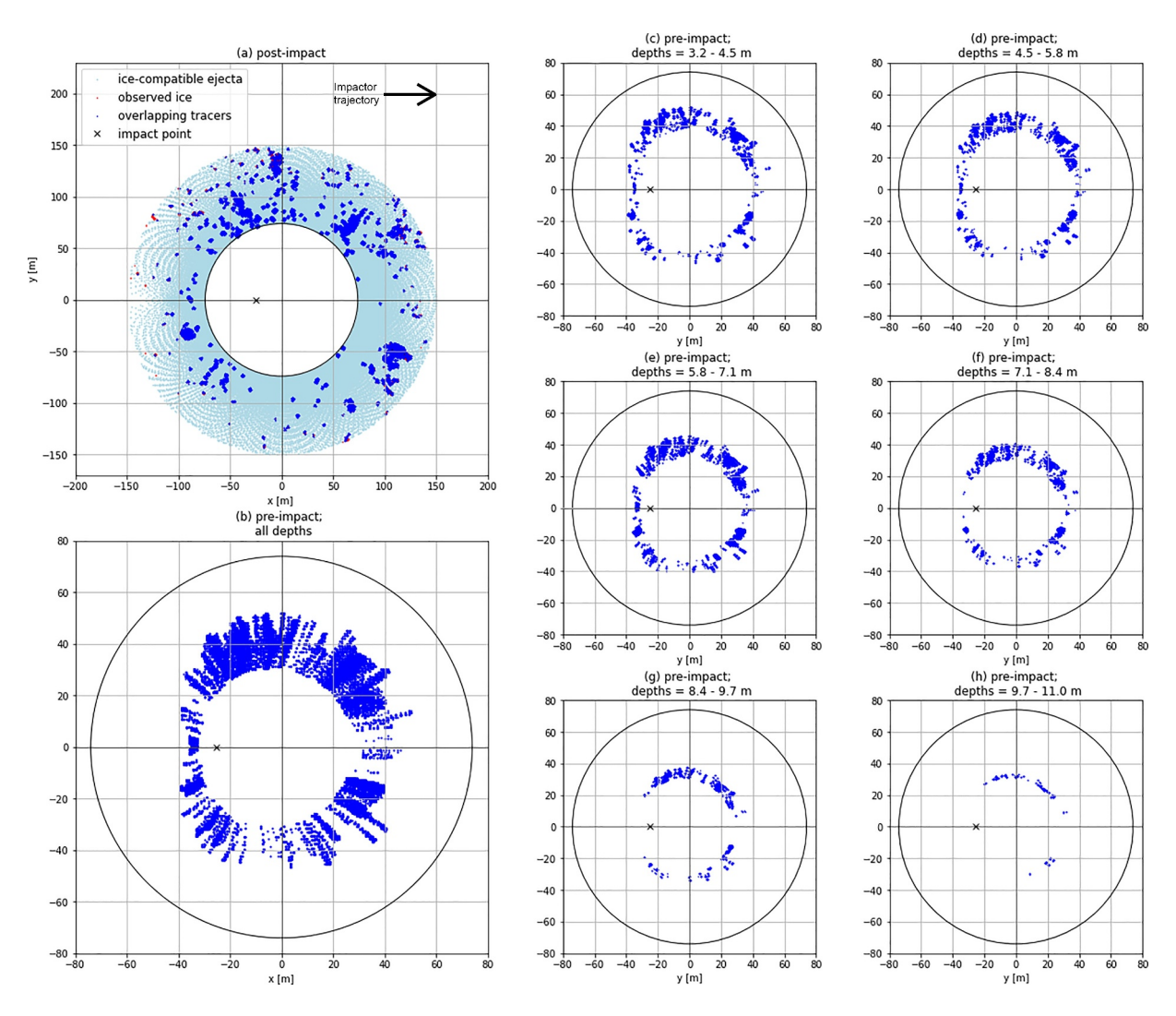


Figure 8. (a) All simulated ice-compatible proximal ejecta at their final projected landing locations (light blue) and the observed ice locations (also in Figures 1b and 1c). Dark blue markers show ice-containing pixels (including ice blocks and patches) overlapping with a simulation tracer and red markers show the pixels with no overlapping tracers. (b) Preimpact locations of simulated ejecta overlapping with observed ice containing pixels (dark blue), originating from depths below 3.2 m. (c–h) Preimpact locations of simulated ejecta overlapping with observed ice pixels originating from 1.3-m-thick depth slices. The black circle shows the approximate observed crater rim and the impact direction is from left to right in all plots.

5. Discussion

Observations of the Christmas Eve crater and other craters in the area suggest that subsurface ice is likely to be in the form of both massive ice (at a depth of several meters) and pore-filling ice (at shallower depths), surrounded by unconsolidated regolith (Dundas et al., 2023). This is consistent with our simulation results that suggest subsurface solid ice is laterally discontinuous at depths of 3.2–11 m. Whilst our simulations do not explicitly include ice, we speculate that the presence of an ice layer in the upper part of the target could result in shallower slopes of the crater walls, bringing it closer to the observed shape. However, the influence of discontinuous patches of ice on the final crater morphology is more difficult to predict. Future studies should therefore investigate the effect on crater formation and material ejection of ice in different forms (e.g., massive ice and pore ice) within the regolith.

Ice blocks visible in orbital images were most likely excavated from the area near the wall of the crater, approximately 30–60 m from crater center. Material in those areas experienced lower temperatures and pressures during the impact than the faster, earlier ejecta, which originated closer to where the impactor contacted and penetrated the target. Though ice could have been present in the penetration zone, it would have been vaporized, melted or crushed during the impact and would not be observed as large blocks in the ejecta blanket.

WÓJCICKA ET AL. 12 of 16

The distribution of ice varies in the cross-range direction. In the observed proximal ejecta, there is ≈4 times more ice (by area) on the northern side of the crater than the southern side. Our simulations were conducted in half-space geometry, where the impactor is assumed to impact along the symmetry plane. Therefore, our results do not consider any cross-range asymmetry in crater morphology or ejecta distribution. The observed asymmetric ice distribution could be the result of lateral variation in preimpact ice distribution under the surface. Alternatively, this asymmetry could be an indication that the topography of the preimpact target generated azimuthal variation in ejection as proposed to explain the production of crater rays (Shuvalov, 2012). For example, a mound on the southern side or a depression on the northern side could explain preferential ejection of material to the north versus the south. Whilst we did not map non-icy ejecta in this work, maps produced by Tusberti et al. (2024) suggest that the distribution of rocky ejecta is approximately azimuthally uniform. This suggests that an uneven subsurface ice distribution is the more likely reason for the asymmetrical ejecta pattern, rather than topography effects. Investigating these hypotheses in detail in the future would require simulations of impact scenarios in full-space geometry that include terrain and subsurface material property variations around the impact point. Such simulations are significantly more computationally expensive than the simulations presented here, and would prohibit varying multiple variables to constrain the impact conditions, as was done here.

The total volume of tracers overlapping observed ice blocks is 1,280 m³, which is equal to 5% of all ejecta from depths 3.2–11 m that lands up to 150 m of the crater center, and $\approx 2\%$ of all material ejected in each of our simulations (see Figure S1 in Supporting Information S1 for volume ejected as a function of time). This small proportion of ejecta landing in the area of interest could indicate that our observational methodology is the most successful at recognizing purest ice, originating from massive ice layers, with significant portion of pore ice going unnoticed. Therefore our volume estimate represents a lower bound for the total ice excavated by the Christmas Eve crater and the true total volume of ice excavated is likely larger.

Our simulations were unable to reproduce the downrange divot observed in the crater rim. The feature is similar to features produced in low-velocity and shallow-angle impact experiments in cohesionless sand, where the impactor ricochets from the target and forms a secondary crater at the rim of the primary crater (Gault & Wedekind, 1978). A similar process observed at shallow impact angles occurs where the impactor is "decapitated"—the impactor is disrupted on impact and a large fragment creates an adjacent secondary crater. However, those features are expected to fall directly downrange, following impactor's trajectory, so this explanation is less likely in this case. Even at the shallow impact angles (as low as 15°) simulated in this work, we do not see evidence of a ricocheting or "decapitated" impactor, though these features were previously reproduced in other numerical simulations of larger impacts (Elbeshausen et al., 2013). We therefore conclude that the "divot" was not formed by impactor ricochet or decapitation. We can also exclude the divot as a pre-existing feature by examining the before and after CTX images (see Figure S2 in Supporting Information S1), where the divot can be seen after the impact, but is not visible before.

We speculate that the divot was instead produced by an impactor fragment that separated during atmospheric entry or as a result of more complex preimpact subsurface layering. Crater clusters are common among recently formed craters (<60 m), accounting for 58% of newly formed craters on Mars (Daubar et al., 2022). Another possible large crater cluster was recently found in Tempe Terra, with the largest of the craters present in the cluster having a diameter of 130 m (Posiolova et al., 2022). In general, impactor fragments fall in ellipse-shaped crater fields. Whilst the size of the original impactor does not affect the initial fragmentation process, as size increases the separation distance between individual craters relative to their diameter decreases. Therefore, for impactors above a critical diameter the craters produced by fragments will overlap. This critical diameter depends on the relative densities of the atmosphere and the projectile, as well as the altitude of fragmentation (Melosh, 1989). For Mars, assuming a nominal break-up altitude of 20 km, that radius is \approx 5 m. This is a little smaller than the impactor diameters in our simulations, which suggests that a fragment impact could be a plausible origin of the divot. If the divot was formed by an impactor fragment separated during atmospheric entry, it would appear that 150 m is at the upper crater size limit of impactors that experience fragmentation in the present-day martian atmosphere, as no larger examples have been observed to date.

6. Conclusions

In this work, we simulated a suite of impact scenarios that could have produced the \sim 150 m diameter Christmas Eve crater on Mars using the iSALE-3D shock physics code. We compared the resulting ejecta distributions and

WÓJCICKA ET AL. 13 of 16

crater morphologies with observations to constrain the most likely impact conditions and simplified target structure, as well as the provenance of icy ejecta.

We considered five possible impact angles between 15° and 45° from horizontal, guided by the observed ejecta and blast-zone features, which suggest a shallow impact angle. The simulated distal ejecta distributions show a forbidden zone in the uprange direction, in agreement with orbital images of the impact blast zone. Impact at an angle of 20° produces a distal ejecta distribution in closest agreement with observations of the blast zone around the Christmas Eve crater, with a consistent uprange forbidden zone opening angle, measured 1–2 km from the crater. Moreover, the edge of the ejecta blanket for the 20° scenario, between 5 and 15 km from the crater, coincides with the scimitar features visible in CTX images of the blast zone. These features were previously hypothesized to be produced by the interaction of the blast wave with the Mach cone. Our results suggest that ejecta blanket emplacement, or the interaction of the ejecta with surface dust and the atmosphere, could be a possible alternative formation mechanism for these features.

Based on the distal ejecta distribution, an impact angle of $20 \pm 2.5^{\circ}$ is the most likely. At this impact angle, and an impact velocity of 12 km/s, the estimated impactor diameter is 6.0 m, with a mass of 9.7×10^5 kg. The impact momentum for this impact scenario is 1.2×10^{10} Ns, and the vertical momentum is 4.0×10^9 Ns. This momentum is slightly larger than that used in previous 2D modeling (Dundas et al., 2023; Posiolova et al., 2022). In this work we did not vary impactor velocity, but if the impactor speed was lower (higher), a larger (smaller) impactor would achieve a similar crater size.

With knowledge of these impact parameters, we were able to constrain the target properties. For an impact angle of 20°, the observed crater morphology was best reproduced by our simulations with a 15 m thick regolith layer overlaying denser and stronger fractured bedrock. This suggests the presence of a stronger layer 15 m under the preimpact surface, which is consistent with observations of other craters in the same area (Dundas et al., 2023).

Together, these results provide a better constrained impact scenario for future studies of seismic wave generation. A key relationship that is not yet fully understood is that between impact parameters and the depth of seismic moment release or source depth (Posiolova et al., 2022). Whilst our simulation domain is too small to investigate the source depth for this impact, the constraints we are able to place on the preimpact target configuration will be invaluable for future studies when combined with the corresponding seismic signal.

We subsequently compared our simulated proximal ejecta distribution with orbital observations of excavated ice blocks, to produce a possible preimpact distribution of subsurface ice. Our simulation results show that the ice blocks visible in orbital images originated from a layer of massive ice at shallow depths between 3.2 and 11 m (potentially with shallower pore ice). This depth can serve as an important equipment constraint for future missions' In-Situ Resource Utilization (ISRU) efforts. Ice blocks were most likely excavated from the area near the wall of the crater, approximately 30–60 m from the crater center. Material in those areas experienced lower temperatures and pressures during the impact than material that originated from near the center of the crater, where pre-existing ice would have been melted or evaporated. The ice was most likely present in a discontinuous pattern, with patches up to 15 m in length depending on depth, and the largest patches originated nearest to the surface (depths 3.2–4.5 m). We estimate the total volume of ice blocks within the proximal ejecta to be $\approx 1,280 \, \text{m}^3$, which represents a lower bound for the total volume of ice excavated by the Christmas Eve crater. Our results are consistent with results indicating that this location is near the limit of shallow extant ice, providing useful constraints for future modeling of ice stability and persistence in this region and is therefore crucial for future climate history studies.

Our work shows how remote sensing and numerical modeling can be used together to constrain site-specific subsurface structure. Our methodology can be applied to other ice-exposing craters in order to help constrain the prevalence and nature of subsurface ice across Mars.

Data Availability Statement

All simulations in this work were performed using iSALE-3D shock physics code and we gratefully acknowledge the developers (https://isale-code.github.io/). iSALE input files used to perform simulations in this work are available at https://doi.org/10.5281/zenodo.14419055 (Wojcicka, 2024). This work used the DiRAC Data Intensive service (DIaL2/DIaL [*]) at the University of Leicester, managed by the University of Leicester

WÓJCICKA ET AL. 14 of 16

Research Computing Service on behalf of the STFC DiRAC HPC Facility (www.dirac.ac.uk). The DiRAC service at Leicester was funded by BEIS, UKRI and STFC capital funding and STFC operations grants. DiRAC is part of the UKRI Digital Research Infrastructure.

Acknowledgments

Any use of trade, firm, or product names is for descriptive purposes only and does not imply endorsement by the U.S. Government. N.W. and G.S.C. were supported by UK Space Agency Grants ST/S001514/1, ST/T002026/1 and ST/ Y000102/1. C.M.D. was funded by NASA MDAP NNH23OB56A. I.J.D. was funded by NASA InSight PS 80NSSC20K0971. V.G.R. was funded by the Alexander von Humboldt Foundation through a postdoctoral fellowship. We thank the editor Debra Buczkowski, and two anonymous reviewers, for providing helpful comments that helped improve this manuscript.

References

- Banerdt, W. B., & Russell, C. T. (2017). Editorial on: Topical collection on InSight mission to Mars. Space Science Reviews, 211(1-4), 1-3. https://doi.org/10.1007/s11214-017-0414-0
- Becker, K. J., Milazzo, M. P., Delamere, W. A., Herkenhoff, K. E., Eliason, E. M., Russell, P. S., et al. (2022). hical—The HiRISE radiometric calibration software developed within the ISIS3 planetary image processing suite Tech. Rep. Reston. https://doi.org/10.3133/tm7C27
- Burleigh, K. J., Melosh, H. J., Tornabene, L. L., Ivanov, B., McEwen, A. S., & Daubar, I. J. (2012). Impact airblast triggers dust avalanches on Mars. *Icarus*, 217(1), 194–201. https://doi.org/10.1016/j.icarus.2011.10.026
- Collins, G. S., Melosh, H. J., & Ivanov, B. A. (2004). Modeling damage and deformation in impact simulations. *Meteoritics & Planetary Sciences*, 39(2), 217–231. https://doi.org/10.1111/j.1945-5100.2004.tb00337.x
- Collins, G. S., Melosh, H. J., & Wünnemann, K. (2011). Improvements to the ε-α Porous compaction model for simulating impacts into high-porosity solar system objects. *International Journal of Impact Engineering*, 38(6), 434–439. https://doi.org/10.1016/j.ijimpeng.2010.10.013
- Daubar, I. J., Dundas, C. M., McEwen, A. S., Gao, A., Wexler, D., Piqueux, S., et al. (2022). New craters on Mars: An updated catalog. *Journal of Geophysical Research: Planets*, 127(7), e2021JE007145. https://doi.org/10.1029/2021JE007145
- Dundas, C. M., Mellon, M. T., Conway, S. J., Daubar, I. J., Williams, K. E., Ojha, L., et al. (2021). Widespread exposures of extensive clean shallow ice in the midlatitudes of Mars. *Journal of Geophysical Research: Planets*, 126(3), 1–28. https://doi.org/10.1029/2020JE006617
- Dundas, C. M., Mellon, M. T., Posiolova, L. V., Miljković, K., Collins, G. S., Tornabene, L. L., et al. (2023). A large new crater exposes the limits of water ice on Mars. Geophysical Research Letters, 50(2), e2022GL100747. https://doi.org/10.1029/2022GL100747
- Durham, W. B., Heard, H. C., & Kirby, S. H. (1983). Experimental deformation of polycrystalline H₂O ice at high pressure and low temperature: Preliminary results. *Journal of Geophysical Research*, 88(S01), B377–B392. https://doi.org/10.1029/JB088iS01p0B377
- Elbeshausen, D., & Wünnemann, K. (2011). ISALE-3D: A three-dimensional, multi-material, multi-rheology hydrocode and its applications to large-scale geodynamic processes. In *Proceedings, 11th hypervelocity impact society symposium*.
- Elbeshausen, D., Wünnemann, K., & Collins, G. S. (2009). Scaling of oblique impacts in frictional targets: Implications for crater size and formation mechanisms. *Icarus*, 204(2), 716–731. https://doi.org/10.1016/j.icarus.2009.07.018
- Elbeshausen, D., Wünnemann, K., & Collins, G. S. (2013). The transition from circular to elliptical impact craters. *Journal of Geophysical*
- Research: Planets, 118(11), 2295–2309. https://doi.org/10.1002/2013JE004477

 Froment, M., Lognonné, P., Larmat, C., Lei, Z., Rougier, E., & Kawamura, T. (2024). Numerical modelling of impact seismic sources using the
- stress glut theory. Geophysical Journal International, 238(1), 156–186. https://doi.org/10.1093/gji/ggae144

 Froment, M., Rougier, E., Larmat, C., Lei, Z., Euser, B., Kedar, S., et al. (2020). Lagrangian-based simulations of hypervelocity impact ex-
- periments on Mars regolith proxy. *Geophysical Research Letters*, 47(13), e2020GL087393. https://doi.org/10.1029/2020GL087393
 Garcia, R. F., Daubar, I. J., Beucler, r., Posiolova, L. V., Collins, G. S., Lognonné, P., et al. (2022). Newly formed craters on Mars located using
- seismic and acoustic wave data from InSight. Nature Geoscience 2022, 10(11), 1–7. https://doi.org/10.1038/s41561-022-01014-0 Gault, D., & Wedekind, J. (1978). Experimental studies of oblique impact. In Lunar and Planetary Science Conference Proceedings, (Vol. 3, pp.
- 3843–3875).
 Grindrod, P. M., Daubar, I. J., Fernando, B., Kim, D., Collins, G. S., Stähler, S. C., et al. (2024). Extensive secondary cratering from the InSight
- Sol 1034a impact event. Journal of Geophysical Research: Planets, 129(12), e2024JE008535. https://doi.org/10.1029/2024JE008535
- InSight Marsquake Service. (2023). Mars seismic catalogue, InSight mission; V14 2023-04-01. ETHZ, IPGP, JPL, ICL, University. Bristol. https://doi.org/10.12686/a21
- Ivanov, B., Barnes, G., Daubar, I., Dundas, C., McEwen, A., & Melosh, J. (2020). New craters on Mars: Air shock wave traces. In Egu general assembly 2020. https://doi.org/10.5194/egusphere-egu/2020-4212
- Kim, D., Banerdt, W. B., Ceylan, S., Giardini, D., Lekić, V., Lognonné, P., et al. (2022). Surface waves and crustal structure on Mars. *Science*, 378(6618), 417–421. https://doi.org/10.1126/science.abq7157
- Lognonné, P., Banerdt, W. B., Giardini, D., Pike, W. T., Christensen, U., Laudet, P., et al. (2019). SEIS: Insight's seismic Experiment for Internal Structure of Mars. Space Science Reviews, 215(1), 12. https://doi.org/10.1007/s11214-018-0574-6
- Lundborg, N. (1968). Strength of rock-like materials. International Journal of Rock Mechanics and Mining Sciences, 5(5), 427–454. https://doi.org/10.1016/0148-9062(68)90046-6
- Malin, M. C., Bell, J. F., Cantor, B. A., Caplinger, M. A., Calvin, W. M., Clancy, R. T., et al. (2007). Context Camera investigation on board the Mars reconnaissance orbiter. *Journal of Geophysical Research*, 112(E5), 5–9. https://doi.org/10.1029/2006JE002808
- McEwen, A. S., Eliason, E. M., Bergstrom, J. W., Bridges, N. T., Hansen, C. J., Delamere, W. A., et al. (2007). Mars reconnaissance orbiter's High Resolution Imaging Science Experiment (HiRISE). *Journal of Geophysical Research*, 112(E5), 5–7. https://doi.org/10.1029/2005JE002605 Melosh, H. J. (1989). Impact cratering: A geologic process. https://doi.org/10.1017/9781316535769.012
- Piqueux, S., Byrne, S., Kieffer, H. H., Titus, T. N., & Hansen, C. J. (2015). Enumeration of Mars years and seasons since the beginning of telescopic exploration. *Icarus*, 251, 332–338. https://doi.org/10.1016/j.icarus.2014.12.014
- Posiolova, L. V., Lognonné, P., Banerdt, W. B., Clinton, J., Collins, G. S., Kawamura, T., et al. (2022). Largest recent impact craters on Mars: Orbital imaging and surface seismic co-investigation. *Science (New York, N.Y.)*, 378(6618), 412–417. https://doi.org/10.1126/science.abq7704 QGIS.org. (2024). QGIS geographic information system. QGIS Association. Retrieved from http://www.qgis.org
- Raducan, S. D., Davison, T. M., & Collins, G. S. (2022). Ejecta distribution and momentum transfer from oblique impacts on asteroid surfaces. *Icarus*, 374, 114793. https://doi.org/10.1016/J.ICARUS.2021.114793
- Rajšić, A., Miljković, K., Collins, G. S., Wünnemann, K., Daubar, I. J., Wójcicka, N., & Wieczorek, M. A. (2021). Seismic efficiency for simple Crater Formation in the Martian top crust analog. *Journal of Geophysical Research: Planets*, 126(2), e2020JE006662. https://doi.org/10.1029/ 2020JE006662
- Rangarajan, V. G., Tornabene, L. L., Osinski, G. R., Conway, S. J., Seelos, F. P., Silvestro, S., et al. (2023). Change detection and monitoring of active Martian surface phenomena with the Colour and Stereo Surface Imaging System (CaSSIS) onboard the ExoMars Trace Gas Orbiter (TGO). *Icarus*, 394, 115443. https://doi.org/10.1016/j.icarus.2023.115443

WÓJCICKA ET AL. 15 of 16

- Rangarajan, V. G., Tornabene, L. L., Osinski, G. R., Dundas, C. M., Beyer, R. A., Herkenhoff, K. E., et al. (2024). Novel quantitative methods to enable multispectral identification of high-purity water ice exposures on Mars using High Resolution Imaging Science Experiment (HiRISE) images. *Icarus*, 419, 115849. https://doi.org/10.1016/j.icarus.2023.115849
- Schultz, P. H., & Gault, D. E. (1979). Atmospheric effects on Martian ejecta emplacement. *Journal of Geophysical Research*, 84(B13), 7669–7687. https://doi.org/10.1029/JB084iB13p07669
- Shuvalov, V. (2012). A mechanism for the production of crater rays. Meteoritics & Planetary Sciences, 47(2), 262–267. https://doi.org/10.1111/j. 1945-5100.2011.01324.x
- Sokołowska, A., Thomas, N., & Wünnemann, K. (2024). Effects of surface and subsurface water/ice on spatial distributions of impact crater ejecta on Mars. *Icarus*, 420, 116150. https://doi.org/10.1016/j.icarus.2024.116150
- Sucharski, T., Mapel, J., jcwbacker, K., Lee, K., Shepherd, M., Stapleton, S., et al. (2020). USGS-Astrogeology/ISIS3: ISIS 4.2.0 public release. Zenodo. https://doi.org/10.5281/zenodo.3962369
- Teanby, N. A., & Wookey, J. (2011). Seismic detection of meteorite impacts on Mars. *Physics of the Earth and Planetary Interiors*, 186(1–2), 70–80. https://doi.org/10.1016/j.pepi.2011.03.004
- Tillotson, J. H. (1962). Metallic equations of state for hypervelocity impacts. Report No. GA-3216. General Atomic. (p. 43) Retrieved from http://oai.dtic.mil/oai/oai?verb=getRecord&metadataPrefix=html&identifier=AD0486711
- Tornabene, L. L., Seelos, F. P., Pommerol, A., Thomas, N., Caudill, C. M., Becerra, P., et al. (2017). Image simulation and assessment of the colour and spatial capabilities of the Colour and Stereo Surface Imaging System (CaSSIS) on the ExoMars trace gas orbiter. *Space Science Reviews*, 214(1), 18. https://doi.org/10.1007/s11214-017-0436-7
- Tusberti, F., Pajola, M., Munaretto, G., Penasa, L., Lucchetti, A., Beccarelli, J., et al. (2024). Ice degradation and Boulder size frequency distribution analysis of the fresh Martian crater S1094b. *Icarus*, 423, 116255. https://doi.org/10.1016/j.icarus.2024.116255
- Wojcicka, N. (2024). nwojcicka/Christmas-crater-ice: Version 1.0.0 [Software]. Zenodo. https://doi.org/10.5281/zenodo.14419055
- Wójcicka, N., Collins, G. S., Bastow, I. D., Teanby, N. A., Miljković, K., Rajšić, A., et al. (2020). The seismic moment and seismic efficiency of small impacts on Mars. *Journal of Geophysical Research: Planets*, 125(10), e2020JE006540. https://doi.org/10.1029/2020JE006540
- Wünnemann, K., Collins, G. S., & Melosh, H. J. (2006). A strain-based porosity model for use in hydrocode simulations of impacts and implications for transient crater growth in porous targets. *Icarus*, 180(2), 514–527. https://doi.org/10.1016/j.icarus.2005.10.013

WÓJCICKA ET AL. 16 of 16